MYU Tokyo

S & M 4466

Investigation of Supercritical Fluid Processing for Nonvolatile Resistive Random Access Memory Devices Based on $SrBi_4Ti_4O_{15}$ Ferroelectric Thin Films

Wen-Lung Lee,[1] Kai-Huang Chen,[*2] Ming-Cheng Kao,[3] Cheng-Che Hsieh,[4] and Chien-Min Cheng[4]

[1]Section of Mathematics and Physics Science, Center for General Education, Air Force Academy, Kaohsiung 82047, Taiwan
[2]Department of Electronic Engineering, Cheng Shiu University. Kaohsiung 83347, Taiwan
[3]Graduate Institute of Aeronautics, Department of Information and Communication Engineering, Chaoyang University of Technology, Taichung 413310, Taiwan
[4]Department of Electronic Engineering, Southern Taiwan University of Science and Technology, Tainan 710301, Taiwan

(Received February 10, 2026; accepted April 20, 2026)

Keywords: supercritical fluid processing, SBT, resistive random access memory, thin films, *I–V*

$SrBi_4Ti_4O_{15}$ (SBT) ferroelectric thin films were fabricated by a sol–gel spin-coating method and evaluated for resistive switching behavior in metal–insulator–metal (MIM) resistive random access memory (RRAM) devices. An SBT precursor solution was deposited on TiN/Si substrates, followed by rapid thermal annealing (RTA) and supercritical fluid (SCF) post-treatments to improve crystallinity, defect passivation, and interfacial quality. The SCF process was performed at 120 °C and 3000 psi using supercritical CO_2 with 0.1 vol.% H_2O. Aluminum top electrodes were deposited to form Al/SBT/TiN/Si structures. X-ray diffraction confirmed the formation of the Aurivillius-type layered perovskite SBT phase with characteristic (119), (200), and (002) orientations. Moderate annealing temperatures yielded uniform grain distribution and reduced defect density, as observed by field-emission scanning electron microscopy. Electrical measurements demonstrated stable bipolar resistive switching with a forming voltage of approximately 6 V and low operating voltages during set/reset processes. The devices exhibited reliable endurance and retention characteristics. Current–voltage fitting revealed ohmic conduction in the low-resistance state owing to conductive filament formation, while Schottky emission and Poole–Frenkel transport dominated the high-resistance state. SCF-treated devices showed reduced leakage current and improved switching uniformity, indicating enhanced dielectric quality. These results demonstrate the feasibility of SBT thin films for low-power nonvolatile memory applications.

[*]Corresponding author: e-mail: 5977@gcloud.csu.edu.tw
https://doi.org/10.18494/SAM6280

ISSN 0914-4935 © MYU K.K.
https://myukk.org/

1. Introduction

Memory technologies can be broadly classified into volatile and nonvolatile memories. Volatile memories store data only while an external power supply is maintained; once the power is removed, the stored information is lost. Representative volatile memories include static random access memory (SRAM) and dynamic random access memory (DRAM). SRAM offers fast access and low power consumption; however, each bit requires six transistors, resulting in relatively low integration density and higher fabrication cost. In contrast, DRAM employs a simpler cell structure consisting of one transistor and one capacitor per bit, enabling higher storage density and lower cost, albeit at the expense of refresh operations and slower access than with SRAM.

Nonvolatile memory (NVM), on the other hand, retains stored information even after the power supply is removed and is therefore widely used for long-term data storage. Conventional nonvolatile memories, such as flash memory and read-only memory (ROM), suffer from inherent limitations including slow read/write and limited endurance. To overcome these drawbacks while combining the advantages of volatile memory with nonvolatile data retention, significant research efforts have been devoted to the development of emerging nonvolatile memory technologies in recent years. These memory technologies are characterized by fast switching, low power consumption, and improved endurance performance.[1–11]

To date, four major types of emerging nonvolatile memories have been extensively investigated: magnetoresistive random access memory (MRAM), phase-change random access memory (PCRAM), ferroelectric random access memory (FeRAM), and resistive random access memory (RRAM). Among these candidates, RRAM has attracted considerable attention owing to its simple metal–insulator–metal (MIM) sandwich structure, which is highly scalable and compatible with three-dimensional stacking, thereby reducing fabrication area and cost while increasing memory density. Compared with other emerging memory technologies, RRAM exhibits several advantages, including low operating voltage, high read speed, and high integration potential.[12–16]

In addition, RRAM offers a broad range of material choices for the resistive switching layer, which can be generally categorized into perovskite-structured and binary oxide materials. In recent years, material research has increasingly focused on rare-earth-based compounds, owing to their rich defect chemistry and promising electrical properties. Thin-film-based resistive switching devices have also been widely explored; however, further optimization is still required to improve endurance and cycling stability. The experimental results reported in the literature demonstrate that MIM-structured RRAM devices can achieve favorable switching ratios, stable resistive states, and reliable operation characteristics. Beyond dielectric layer engineering, the metal–dielectric interface in the MIM structure plays a critical role in determining the overall performance of RRAM devices. Consequently, extensive efforts have been devoted to tailoring electrode materials and contact properties to further enhance switching behavior, reliability, and device uniformity.[17–27]

2. Experimental Details

In this experiment in Fig. 1, a home-prepared $SrBi_4Ti_4O_{15}$ (SBT) precursor solution was synthesized by the sol–gel method. The starting materials included strontium acetate [$Sr(CH_3COO)_2$, 99.9%], bismuth nitrate pentahydrate [$Bi(NO_3)_3 \cdot 5H_2O$, 99.3%], titanium isopropoxide [$Ti\{OCH(CH_3)_2\}_4$, 97%], acetic acid (CH_3COOH, 99.9%), ethylene glycol ($HOCH_2CH_2OH$, 99.3%), and acetylacetone ($C_5H_8O_2$, 99%). Initially, strontium acetate and bismuth nitrate pentahydrate were separately dissolved in acetic acid and ethylene glycol, respectively, at a molar ratio of 1:10, and stirred at room temperature for 30 min. Subsequently, titanium isopropoxide was mixed with acetylacetone at a molar ratio of 1:10 and stirred for 30 min to form a stabilized titanium precursor solution. This titanium-containing solution was then slowly added dropwise into the previously prepared mixed solution under continuous stirring, followed by further stirring for 40 min to ensure homogeneous mixing. Finally, the resulting SBT precursor solution was heated to 60 ℃ and stirred for 1 h using a rotary evaporator to promote solvent evaporation and solution stabilization. The prepared solution was then allowed to age at room temperature for 24 h prior to thin-film deposition.

In this study, SBT thin films were deposited on TiN/Si substrates by the sol–gel spin-coating technique. To improve film quality through defect passivation, structural reordering, and recrystallization, two post-treatment approaches—rapid thermal annealing (RTA) and supercritical fluid (SCF) processing—were employed. Subsequently, aluminum (Al) top electrodes were formed to construct MIM resistive memory devices exhibiting ferroelectric characteristics. For the supercritical treatment, the fabricated thin-film RRAM devices were placed in an SCF system and processed at 120 ℃ for 1 h under a pressure of 3000 psi, using supercritical CO_2 ($SCCO_2$) mixed with 0.1 vol.% deionized H_2O. After post-treatment, an Al top electrode with a thickness of 500 nm was deposited onto the SBT thin film by DC magnetron sputtering, forming a complete MIM sandwich structure.

The current–voltage (*I*–*V*) characteristics of the RRAM devices were measured using an Agilent B1500 semiconductor parameter analyzer in conjunction with a Cascade M150 microprobe station. The crystalline structure and surface morphology of the insulating layer were examined by X-ray diffraction (XRD) and field-emission (FE)-SEM, respectively.

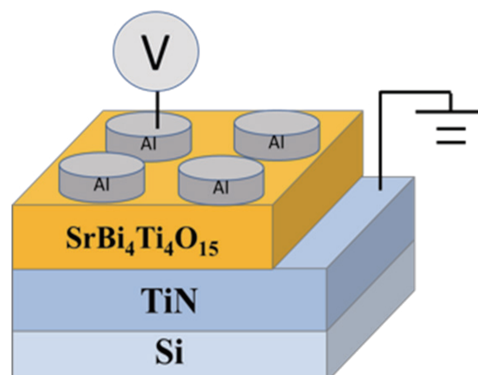

Fig. 1. (Color online) MIM structure of SBT-film RRAM devices.

3. Results and Discussion

Figure 2 shows the XRD patterns of SBT thin films annealed at temperatures ranging from 400 to 600 ℃. Distinct diffraction peaks are consistently observed at approximately $2\theta = 27$, 36, and 45°, which can be indexed to the (119), (200), and (002) planes of the Aurivillius-type layered perovskite structure, respectively. The presence of these characteristic reflections confirms the successful formation of the SBT phase under all annealing conditions. The (119) and (200) orientations indicate the establishment of a well-developed layered perovskite framework, while the (002) peak suggests partial *c*-axis preferential orientation, a typical feature of Bi-layered

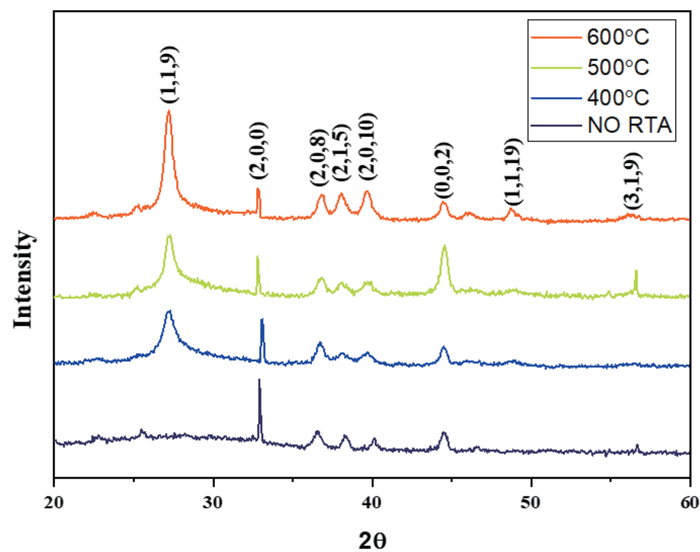

(a)

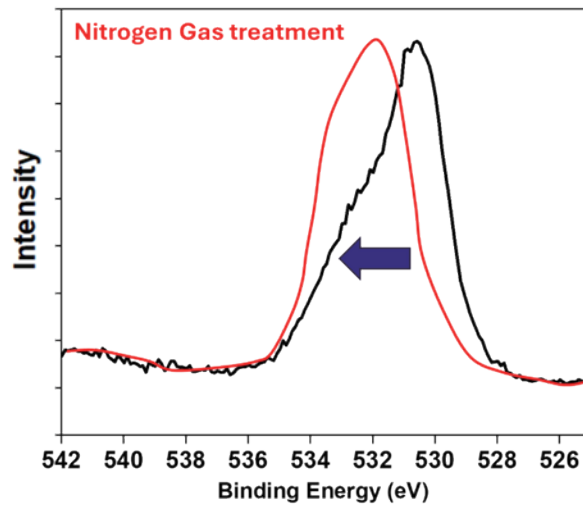

(b)

Fig. 2. (Color online) (a) X-ray diffraction patterns of SBT oxide films at different annealing temperatures and (b) XPS measurement of SBT oxide films subjected to nitrogen gas $SCCO_2$ treatment.

oxide systems. With increasing annealing temperature, the diffraction peaks become sharper and exhibit higher intensities, indicating enhanced crystallinity and reduced lattice disorder. This improvement is attributed to increased atomic diffusion at elevated temperatures, which facilitates grain growth and long-range ordering within the SBT lattice. Notably, the retention of identical major diffraction peaks across different annealing temperatures demonstrates the structural stability of the SBT phase, whereas variations in peak intensity reflect differences in the degree of crystallization. These structural evolutions are in good agreement with the surface morphology trends observed by SEM and play a critical role in enhancing the electrical performance of SBT-based RRAM devices, as higher crystallinity generally results in a more uniform defect distribution and more stable resistive switching pathways, as illustrated in Fig. 3.

The XPS spectrum reveals a clear chemical shift after the nitrogen-assisted SCF treatment of SBT thin films. Compared with the untreated sample, the oxygen core-level peak shifts toward low binding energy, indicating modified electronic states and reduced defect density. This shift suggests successful oxygen incorporation, which alters the local bonding environment and passivates oxygen-vacancy-related traps. The presence of oxygen-related bonding further

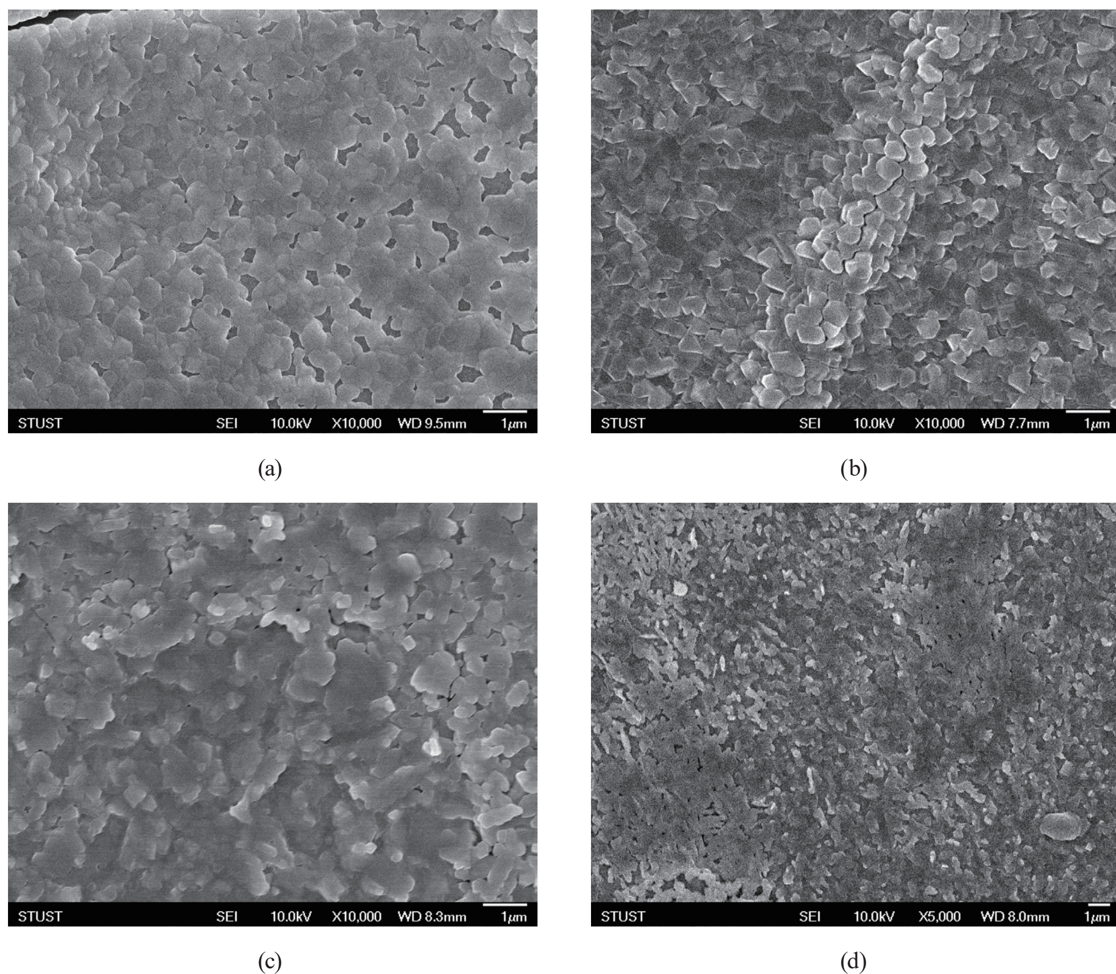

Fig. 3. Surface morphology of SBT oxide thin films treated at different annealing temperatures: (a) nontreated, and (b) 400, (c) 500, and (d) 600 °C.

stabilizes the lattice and suppresses charge trapping effects. Consequently, the SCF-treated SBT films exhibit improved electrical stability and reduced leakage current, confirming the effectiveness of SCF nitridation in defect engineering.

The surface morphologies of SBT thin films annealed at different temperatures are presented in Fig. 3. The as-deposited SBT film exhibits an amorphous surface morphology without discernible grain features, accompanied by pronounced pores and structural defects, which can be attributed to insufficient atomic mobility to support crystallization. After annealing at 400 °C, the onset of perovskite-phase nucleation, indicated by the formation of fine grains while maintaining a relatively smooth surface, is observed. When the annealing temperature is increased to 500 °C, enhanced atomic diffusion promotes uniform grain growth and improved film densification, leading to a substantial reduction in defect density and indicating the optimal crystallization of the sol–gel-derived SBT film. In contrast, annealing at 600 °C results in excessive thermal activation, causing abnormal grain growth, partial grain melting, and increased surface roughness. This degradation behavior is likely related to the volatility of Bi-containing layered perovskite structures at elevated temperatures. Overall, the microstructural evolution suggests that annealing at 400 °C provides an effective balance between crystallization and microstructural stability, yielding a well-defined grain structure that is expected to improve the reliability and uniformity of resistive switching in Al/SBT/TiN/Si MIM devices.

Figure 4(a) shows the forming, set, and reset characteristics of the SBT-oxide-based RRAM devices. An initial forming process was required to induce conductive filament formation within the SBT oxide layer under a sufficiently high electric field. This forming operation was accomplished by applying a voltage of approximately 4 V, thereby establishing a stable conductive pathway through the insulating film. During the set process, the device switched from the high-resistance state (HRS) to the low-resistance state (LRS) when a negative bias exceeding the set voltage was applied. In contrast, the reset process involved a transition from

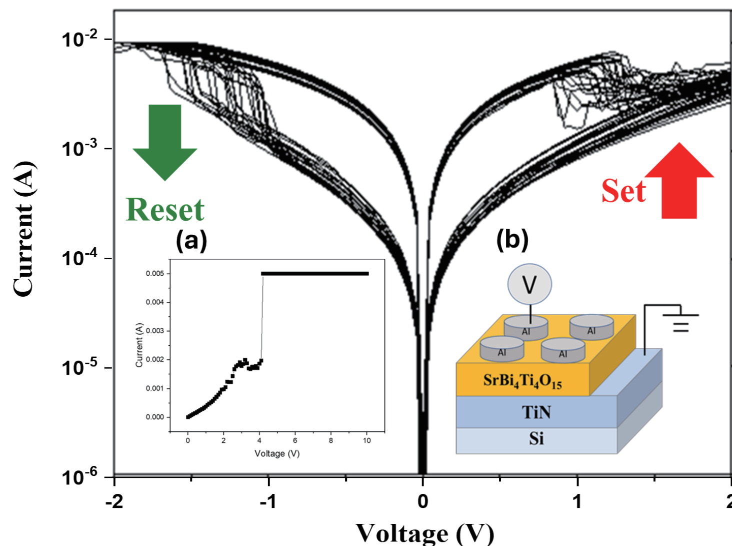

Fig. 4. (Color online) *I*–*V* curves of SBT oxide film RRAM devices for (a) the initial forming process and (b) the Al/SBT/TiN/Si structure for 100 measurements.

the LRS back to the HRS upon the application of a positive bias higher than the reset voltage, accompanied by a gradual decrease in current owing to the partial rupture of the conductive filament. To evaluate the switching reliability, consecutive set/reset cycling was conducted for 100 cycles on the RRAM devices, as shown in Fig. 4(b). A current compliance of 10 mA was employed throughout the measurements to suppress irreversible dielectric breakdown. The extracted set and reset voltages were both approximately −0.5 V, indicating highly stable and reproducible bipolar resistive switching behavior in the SBT-oxide-based RRAM devices.

To further elucidate the electrical transport behavior in the set state, the dominant conduction mechanisms were systematically analyzed through *I–V* curve fitting. SBT-oxide-based RRAM devices with various oxygen contents were fabricated to investigate the effects of SCF processing ($SCCO_2$) on different gas characteristics. On the basis of the fitting results, multiple conduction models—including ohmic conduction, Schottky emission, and Poole–Frenkel transport—were identified and discussed to describe the carrier transport behavior under different electric field regimes.

The electrical current density of the ohmic conduction mechanism is

$$J = E_i exp\left(\frac{-\Delta E_{ac}}{kT}\right), \tag{1}$$

where E_i is the electric field in the insulator, ΔE_{ac} is the electron activation energy, k is the Boltzmann constant, and T is temperature.[28-31]

The electrical current density of the Schottky conduction mechanism is written as

$$J = A^* T^2 \exp\left[\frac{-q\left(\phi_B - \sqrt{\frac{qE}{4\pi\varepsilon_i}}\right)}{kT}\right], \tag{2}$$

where A^* is the effective Richardson constant, T is temperature, k is the Boltzmann constant, E is the electric field in the insulator, ϕ_B is the Schottky barrier height, q is the electronic charge, and ε_i is the dielectric constant

The electrical current density of the Poole–Frankel conduction mechanism is

$$J = \frac{9\varepsilon_i u V^2}{8d^3} = \left(\frac{9\varepsilon_i u}{8d^3}\right) E_i^2, \tag{3}$$

where ε_i is the dielectric constant, u is the carrier mobility, d is the insulator thickness, E_i is the electric field, and V is the voltage across the insulator.[28–31]

The electrical characteristics of the SBT film RRAM devices were analyzed as a function of annealing temperature. Since the as-deposited devices did not exhibit a discernible memory window, the conduction mechanism analysis of the nonannealed samples is not included in this

section. Figure 5 shows the fitting results for the current conduction mechanism of devices annealed at 400 °C. The *I*–*V* data were reorganized according to Eq. (1) and plotted in the form of ln(*I*) versus ln(*V*).(28–31) A fitted slope close to unity indicates ohmic conduction behavior. From the fitting results, ohmic conduction was identified to be the dominant transport mechanism in the HRS at low applied voltages. Similarly, the conduction behavior in the LRS was analyzed using the same ln(*I*)–ln(*V*) fitting approach derived from Eq. (1).(28–31) The linear relationship observed in the ln(*I*)–ln(*V*) plot confirms that ohmic conduction also governs charge transport in the LRS, indicating the presence of stable conductive paths formed within the insulating layer after the switching process.

Figure 5(b) shows the fitting results for the conduction mechanism of the RRAM devices annealed at 500 °C. The *I*–V characteristics were reorganized in accordance with Eqs. (1)–(3) and plotted as ln(*I*) versus ln(*V*). A fitting slope close to unity is indicative of ohmic conduction. From the fitting analysis, both the HRS and LRS exhibit ohmic conduction behavior over the measured voltage range, suggesting the formation of stable and uniform conductive paths within the insulating layer at this annealing temperature.

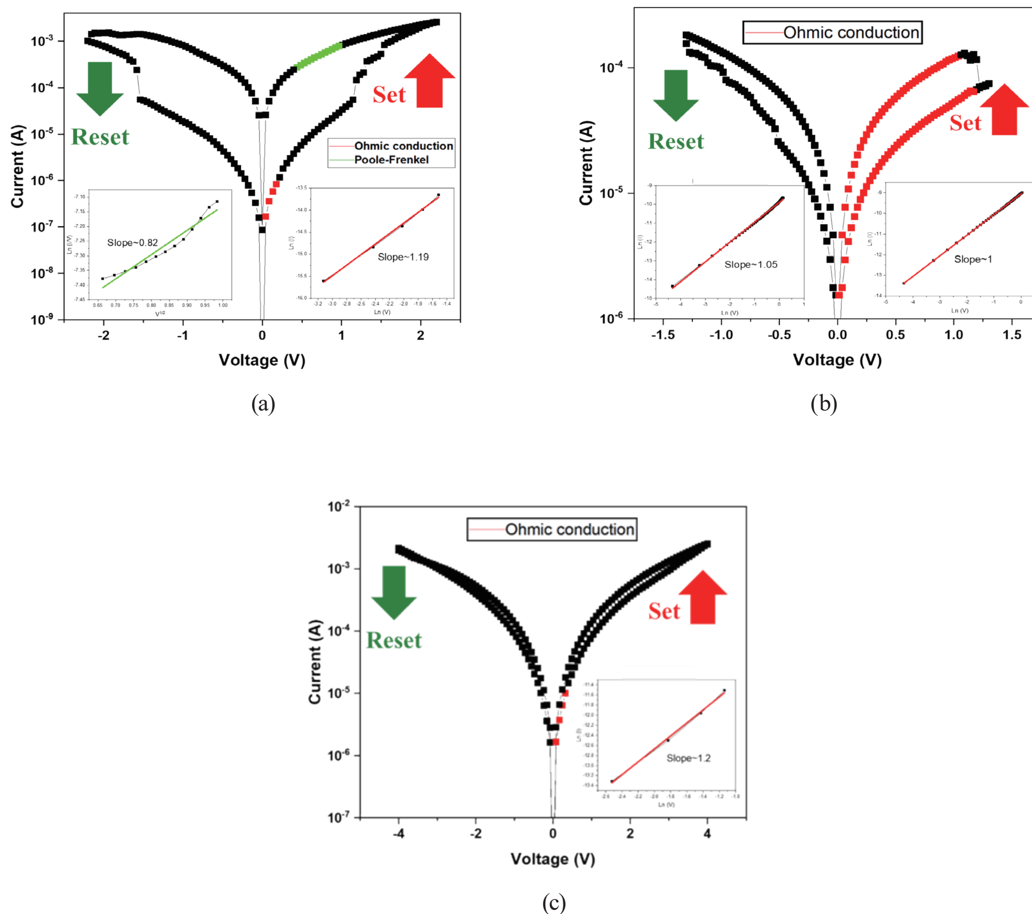

Fig. 5. (Color online) *I*–*V* curves and electrical conduction mechanism of SBT oxide film RRAM devices for (a) 400 °C, (b) 500 °C, and (c) 600 °C annealing treatment.

Figure 5(c) shows fitting results for the conduction mechanism of the devices annealed at 600 °C. Again, the *I*–*V* data were analyzed using the ln(*I*)–ln(*V*) representation derived from Eqs. (1)–(3). The linear fitting observed in the low-voltage region indicates ohmic conduction behavior. The analysis reveals that the HRS is dominated by ohmic conduction at low applied voltages, implying that residual conductive pathways or thermally activated carriers contribute to charge transport after high-temperature annealing.

Figure 6 shows the *I*–*V* characteristics of Al/SBT(H_2O–$SCCO_2$)/TiN RRAM devices processed at different temperatures under a constant pressure of 3000 psi. As shown in Fig. 6, the device treated at 90 °C exhibits a reversal between the HRS and the LRS during the SET process, resulting in an on/off ratio below unity. In contrast, when the treatment temperature is increased to 120 °C, as illustrated in Fig. 6, the on/off ratio significantly improves to approximately 9. This enhancement is attributed to the incorporation of H_2O molecules into the SBT thin film during supercritical processing, which facilitates hydration reactions at grain boundaries and effectively passivates internal defects, thereby suppressing leakage current. A comparative analysis in Fig. 6 confirms that 120 °C is the optimal supercritical treatment temperature for the Al/SBT(H_2O–$SCCO_2$)/TiN devices.

Figure 7 shows the fitting results for the conduction mechanism of the Al/SBT(H_2O–$SCCO_2$)/TiN devices. For the sample treated at 90 °C [Fig. 7(a)], the *I*–*V* data were analyzed using the ln(*I*)–ln(*V*) representation derived from Eqs. (1)–(3), where a fitting slope close to unity indicates ohmic conduction. The fitting results reveal that both the HRS and the LRS are dominated by ohmic conduction. In contrast, for the device treated at 120 °C [Fig. 7(b)], the HRS exhibits unstable resistive behavior, preventing reliable conduction analysis. However, the LRS still shows a linear ln(*I*)–ln(*V*) relationship, confirming ohmic conduction in the LRS.

Figure 8 shows the conduction mechanism fitting results for the conduction mechanism of the Al/SBT(N_2–$SCCO_2$)/TiN device treated at 120 °C. As observed in Fig. 8, the devices without nitrogen incorporation exhibit predominantly ohmic conduction behavior. However, after N_2–$SCCO_2$ treatment, the *I*–*V* characteristics were analyzed using the ln(*I*) versus $V^{1/2}$ representation

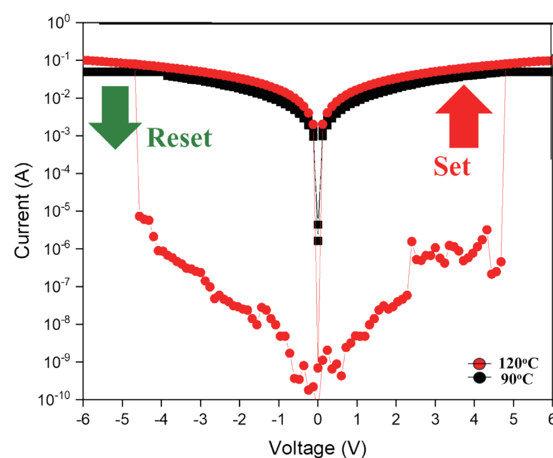

Fig. 6. (Color online) *I*–*V* curves and electrical conduction mechanism of SBT oxide film RRAM devices during $SCCO_2$ treatment using hydrogen gas.

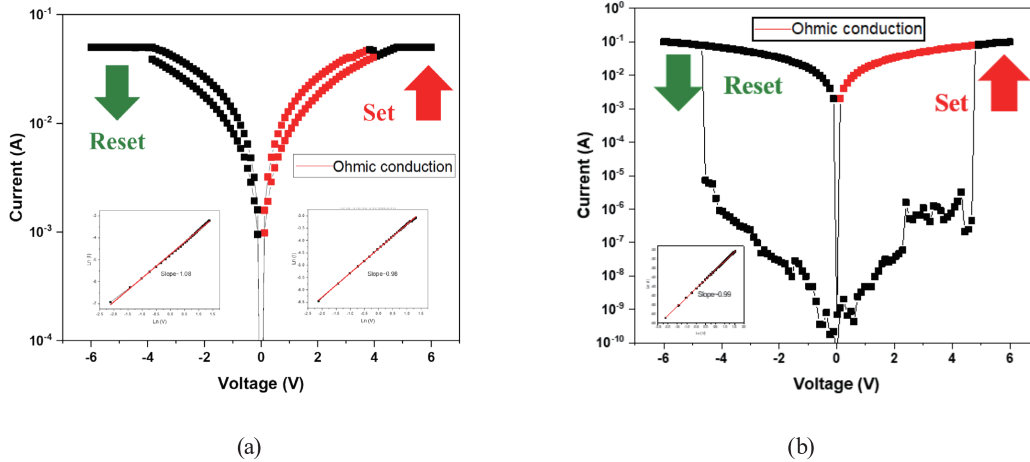

Fig. 7. (Color online) I–V curves and electrical conduction mechanism of SBT oxide film RRAM devices with $SCCO_2$ treatment using hydrogen gas at (a) 90 and (b) 120 °C.

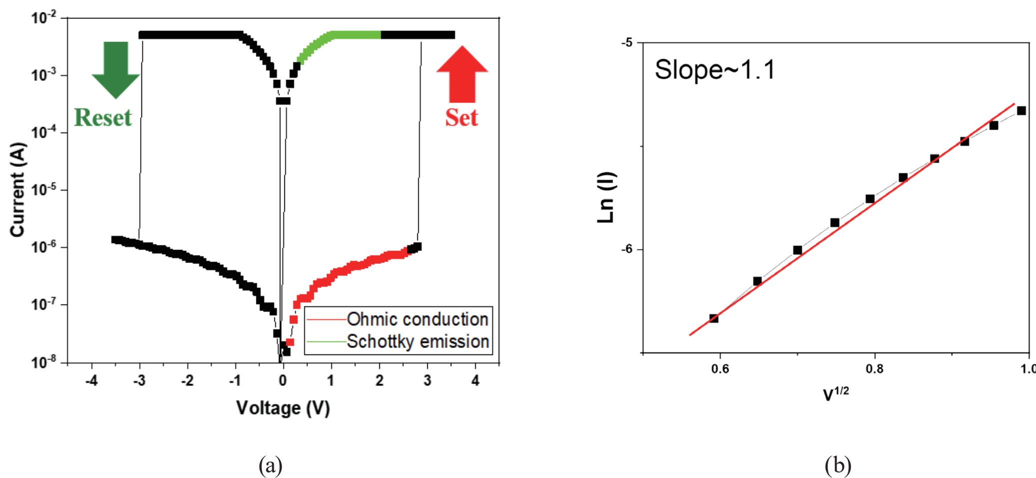

Fig. 8. (Color online) (a) I–V curves and (b) electrical conduction mechanism of SBT oxide film RRAM devices with $SCCO_2$ treatment using nitrogen gas at 120 °C.

derived from Eqs. (1)–(3). The linear fitting indicates that nitrogen incorporation into the SBT thin film modifies the carrier transport mechanism. The diffused nitrogen atoms facilitate thermally activated electron transport by enabling carriers to overcome the interfacial energy barrier, resulting in a transition from ohmic conduction to Schottky-emission-dominated behavior.

Figure 9 shows the endurance characteristics of the RRAM devices subjected to RTA at 400 °C and Al/SBT(N_2–$SCCO_2$)/TiN treatment at 120 °C. The results clearly indicate that the introduction of nitrogen during the SCF process significantly enhances device reliability. Compared with the RTA-treated device, the N_2–$SCCO_2$-treated device exhibits a lower and more stable leakage current in both the HRS and the LRS throughout repeated switching cycles.

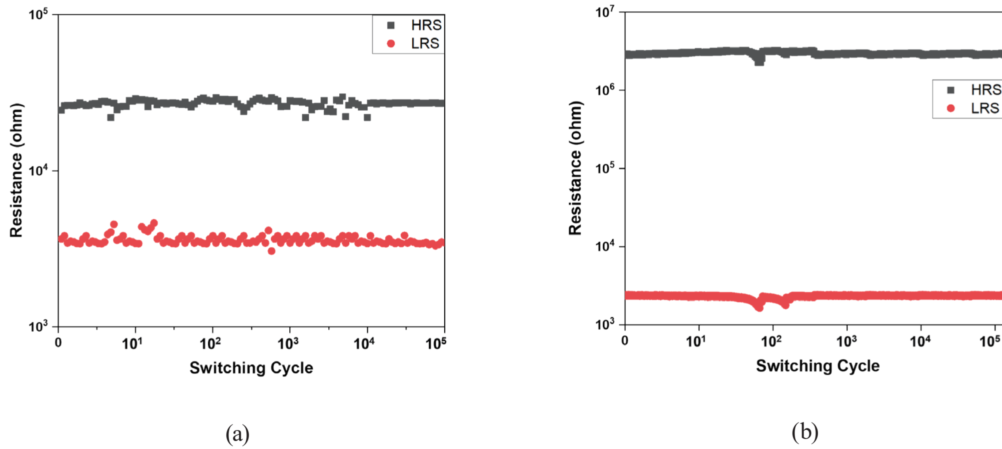

Fig. 9. (Color online) Resistance versus switching cycle curves of SBT oxide film RRAM devices (a) nontreated and (b) with 120 °C N_2 $SCCO_2$ treatment.

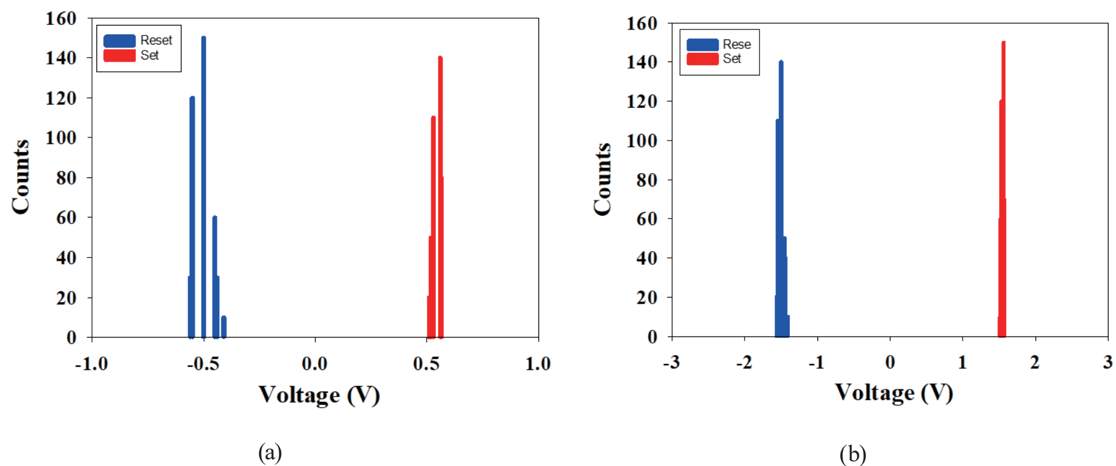

Fig. 10. (Color online) Switching voltage distribution of SBT oxide film RRAM devices (a) nontreated and (b) with 120 °C N_2 $SCCO_2$ treatment.

The improved endurance performance is attributed to the incorporation of nitrogen into the SBT thin film, which effectively suppresses oxygen ion diffusion and stabilizes defect states within the insulating layer. By limiting the migration of oxygen vacancies during repeated switching operations, the conductive filament formation and rupture processes become more controllable, thereby enabling the reduction of current fluctuation and the prevention of premature degradation. As a result, the Al/SBT(N_2–$SCCO_2$)/TiN device demonstrates enhanced switching uniformity and a marked increase in the number of consecutive operation cycles. These findings confirm that nitrogen-assisted SCF treatment is effective for improving leakage suppression and endurance reliability in SBT-based RRAM devices, making it a promising post-treatment technique for high-stability nonvolatile memory applications.

Figures 10(a) and 10(b) show the statistical distributions of set and reset voltages for SBT-based RRAM devices before and after SCF treatment. For the as-deposited device, the set and reset voltages are centered around −0.5 and 0.5 V, respectively, with a relatively narrow switching window. This limited voltage margin suggests unstable filament formation, likely caused by a high density of defects and oxygen vacancies in the untreated SBT film. After SCF treatment, the set and reset voltages shift to approximately −1.5 and +2 V, respectively, resulting in a significantly enlarged switching window. The increased voltage separation indicates improved distinction between the HRS and the LRS, which is beneficial for reliable device operation. In addition, the voltage distributions remain relatively concentrated, suggesting enhanced switching uniformity.

The improvement is attributed to defect passivation and structural reorganization induced by SCF processing, which suppresses the formation of oxygen-vacancy-related leakage paths and stabilizes conductive filament dynamics. Consequently, higher and more stable switching voltages are required, reflecting improved dielectric quality. Overall, SCF treatment effectively enhances the switching stability, voltage margin, and device reliability in SBT-based RRAM devices.

5. Conclusions

In this study, SBT thin films were successfully fabricated on TiN/Si substrates by a sol–gel spin-coating technique and employed as the insulating layer in MIM RRAM devices with aluminum top electrodes. The effects of annealing temperature and low-temperature SCF post-treatment on the structural, electrical, and conduction characteristics of the SBT films were systematically investigated to identify optimal processing conditions.

The Al/SBT/TiN devices annealed at 400 ℃ exhibited the highest performance among the thermally treated samples, showing an on/off resistance ratio of approximately 2, a leakage current density of about 10^{-5} A/cm^2, and stable switching endurance over ~125 consecutive cycles. Conduction mechanism analysis revealed that charge transport in these devices was dominated by ohmic conduction, indicating the formation of stable conductive paths within the SBT layer.

Further performance enhancement was achieved through nitrogen-assisted supercritical CO_2 treatment at 120 ℃ and 3000 psi. The Al/SBT(N_2–$SCCO_2$)/TiN devices demonstrated a significantly improved on/off ratio of approximately 5, a reduced leakage current density of ~10^{-6} A/cm^2, and a markedly enhanced endurance exceeding 500 switching cycles. The incorporation of nitrogen into the SBT thin film effectively restricted oxygen ion diffusion by trapping oxygen species near conductive filaments, leading to improved switching stability. As a result, the dominant conduction mechanism transitioned from ohmic conduction to Schottky emission, attributed to thermally activated carrier transport across a stabilized interfacial energy barrier.

Overall, the introduction of nitrogen—owing to its chemical similarity to oxygen—preserves the intrinsic ferroelectric characteristics of SBT while enhancing device stability and suppressing

leakage current. The low-temperature SCF nitridation process provides an effective and scalable route for defect engineering in SBT-based RRAM devices, highlighting its potential for reliable, low-power nonvolatile memory applications.

Acknowledgments

This work was performed at the National Science Council Core Facilities Laboratory for Nano-Science and Nano-Technology in the Kaohsiung-Pingtung area and was supported by the National Science Council of the Republic of China under Contract No. NSTC 113-2622-E-230-001.

References

1 L. Li, T. J. Dai, K. Liu, K. C. Chang, R. Zhang, X. Lin, H. J. Liu, Y. C. Lai, and T. P. Kuo: Nanoscale **13** (2021) 14035.
2 L. Li, K. C. Chang, R. Zhang, X. Lin, Y. C. Lai, and T. P. Kuo: Nanoscale **12** (2020) 15721.
3 L. Li, K. C. Chang, C. Ye, X. Lin, R. Zhang, Z. Xu, W. Xiong, Y. Zhou, and T. P. Kuo: Nanoscale **12** (2020) 3267.
4 K. C. Chang, T. J., Dai, L. Li, X. N. Lin, S. D. Zhang, Y. C. Lai, H. J. Liu, and Y. E. Syu: Nanoscale **12** (2020) 22070.
5 K. C. Chang, R. Zhang, T. C. Chang, T. M. Tsai, T. J. Chu, H. L. Chen, C. C. Shih, C. H. Pan, Y. T. Su, and P. J. Wu: IEEE Int. Electron Devices Meeting (IEDM 2014) 33.
6 C. Ye, Z. Xu, K. C. Chang, L. Li, X. N. Lin, R. Zhang, Y. Zhou, W. Xiong, and T. P. Kuo, Nanoscale **11** (2019) 20792.
7 M. Lanza, R. Waser, D. Ielmini, J. J. Yang, L. Goux, J. Suñe, A. J. Kenyon, A. Mehonic, S. Spiga, V. Rana, S. Wiefels, S. Menzel, I. Valov, M. A. Villena, E. Miranda, X. Jing, F. Campabadal, M. B. Gonzalez, F. Aguirre, F. Palumbo, K. Zhu, J. B. Roldan, F. M. Puglisi, L. Larcher, T.-H. Hou, T. Prodromakis, Y. Yang, P. Huang, T. Wan, Y. Chai, K. L. Pey, N. Raghavan, S. Dueñas, T. Wang, Q. Xia, and S. Pazos: ACS Nano **15** (2021) 17214. https://doi.org/10.1021/acsnano.1c06980
8 A. Sebastian, M. Le Gallo, R. Khaddam-Aljameh, and E. Eleftheriou: Nat. Nanotechnol. **15** (2020) 529.
9 A. Sebastian, M. Le Gallo, R. Khaddam-Aljameh, C. Funck, and S. Menzel: ACS Appl. Electron. Mater. **3** (2021) 3674.
10 T. Dalgaty, N. Castellani, C. Turck, K. E. Harabi, D. Querlioz, and E. Vianello: Nat. Electron. **4** (2021) 151.
11 M. Lanza, H. S. P. Wong, E. Pop, D. Ielmini, D. Strukov, B. Regan, L. Larcher, M. Villena, J. Yang, and L. Goux: Adv. Electron. Mater. **5** (2019) 1800143.
12 K. H. Chen, C. M. Cheng, N. F. Wang, H. W. Hung, C. Y. Li, and S. Wu: Nanomaterials **13** (2023) 198. https://doi.org/10.3390/nano13010198
13 T. M. Tsai, K. C. Chang,; T. C. Chang, R. Zhang, T. Wang, C. H. Pan, K. H. Chen, H. M. Chen, M. C. Chen, and Y. T. Tseng: IEEE Electron. Device Lett. **37** (2016) 408. https://doi.org/10.1109/LED.2016.2532883
14 R. Zhang, T. F. Young, M. C. Chen, H. L. Chen, S. P. Liang, Y. E. Syu, S. M. Sze, K. C. Chang, T. C. Chang, and T. M. Tsai: IEEE Electron. Device Lett. **35** (2014) 630. https://doi.org/10.1109/LED.2014.2316806
15 C. Y. Lin, K. C. Chang, T. C. Chang, T. M. Tsai, C. H. Pan, R. Zhang, K. H. Liu, H. M. Chen, Y. T. Tseng, and Y. C. Hung: IEEE Electron. Device Lett. **36** (2015) 564. https://doi.org/10.1109/LED.2015.2424226
16 C. H. Jung, S. I. Woo, Y. S. Kim, and K. S. No: Thin Solid Films **519** (2001) 3291.
17 W. W. Zhuang, W. Pan, B. D. Ulrich, J. J. Lee, L. Stecker, A. Burmaster, D. R. Evans, S. T. Hsu, M. Tajiri, and A. Shimaoka: Int. Electron Devices Meeting **8** (2002) 193.
18 N. Raghavan, K. L. Pey, W. Liu, X. Wu, X. Li, and M. Bosman: Microelectron. Eng. **88** (2011) 1124.
19 G. Rajendran, W. Banerjee, A. Chattopadhyay, and M. M. S. Aly: Adv. Electron. Mater. **7** (2021) 2100536. https://doi.org/10.1002/aelm.202100536
20 Z. Miao, L. Chen, F. Zhou, and Q. J Wang: J. Phys. D: Appl. Phys. **51** (2017) 2.
21 Z. Yan, Y. Guo, and G. Zhang: Adv. Mater. **23** (2011) 1351.
22 X. Wu, Z. Xu, F. Zhao, X. Xu, B. Liu, T. Sun, S. Liu; W. Zhao, and Z. Ma: J. Alloys Compd. **602** (2014) 175.
23 N. N. Ge, C. H. Gong, X. C. Yuan, H. Z. Zeng, and X. H. Wei: RSC Adv. **8** (2018) 29499.

24 X. Zhang, X. Chen, J. P. Cao, H. W. Wang, W. Y. Deng, L. H. Yang, K. Lin, Q. Li, Q. H. Li, and Y. L. Cao: Nanoscale. **6** (2024) 3081.
25 S. F. Wang,;Y. C. Wu, Y. G. Hsu, J. P. Chu, and C. H Wu: J. Appl. Phys. **46** (2007) 2978.
26 H. Itoh, H. Asano, K. Fukuroi, M. Nagata, and H. J. Iwahara: Am. Ceram. Soc. **80** (1997) 1359.
27 C. Walczyk, D. Walczyk, T. Schroeder, T. Bertaud, M. Sowin, M. Lukosius, M. Fraschke, D. Wolansky, B. Tillack, and E. Miranda: IEEE Trans. Elect. Dev. **58** (2011) 3124.
28 K. H. Chen, C. M. Cheng, N. F. Wang, H. W. Hung, C. Y. Li, and S. Wu: Nanomaterials **13** (2023) 2179.
29 T. M. Tsai, K. C. Chang, T. C. Chang, R. Zhang, T. Wang, C. H. Pan, K. H. Chen, H. M. Chen, M. C. Chen, and Y. T. Tseng: IEEE Electron. Device Lett. **37** (2016) 408.
30 R. Zhang, T. F. Young, M. C. Chen, H. L. Chen, S. P. Liang, Y. E. Syu, S. M. Sze, K. C. Chang, T. C. Chang, and T. M. Tsai: IEEE Electron. Device Lett. **35** (2014) 630. https://doi.org/10.1109/LED.2014.2316806
31 K. C. Chang, T. C. Chang, T. M. Tsai, R. Zhang, Y. C. Hung, Y. E. Syu, Y. F. Chang, M. C. Chen, T. J. Chu, and H. L. Chen: Nano Rev. **10** (2015) 120.